Simple Active Damping Solution for Industrial Grid-Tied Inverters Using LCL Filters

Simple Active Damping Solution for Industrial Grid-Tied Inverters using LCL Filters

Alessia Camboni
Dipartimento Energia "G. Ferraris"
Politecnico di Torino
Torino, Italy
alessia.camboni@polito.it

Alessandro Roveri
Prima Electro S.p.A.
Moncalieri, Italy
alessandro.roveri@primaelectro.com

Fabio Mandrile
Dipartimento Energia "G. Ferraris"
Politecnico di Torino
Torino, Italy
fabio.mandrile@polito.it

Radu Bojoi
Dipartimento Energia "G. Ferraris"
Politecnico di Torino
Torino, Italy
radu.bojoi@polito.it

***Abstract*—Grid-tied power inverters are typically interfaced with damped LC or LCL filters to limit the injection of switching harmonics. To minimize filter losses, the damping resistance of the filter is often reduced, resulting in poorly damped or unstable conditions at the resonant frequency. Therefore, different active damping solutions have been proposed in the literature to reduce passive elements while avoiding unstable conditions. However, most available solutions require additional current sensors or implement complex active damping algorithms. Moreover, the literature provides only partial guidelines to tune the active damping parameters. Therefore, this paper proposes a sensorless active damping solution based on a resonant current estimator and provides a straightforward tuning for its parameters. The proposed active damping method is experimentally tested on a three-phase, two-level 30 kVA inverter, thus demonstrating the validity of the presented approach.**

***Index Terms*—LCL Filter, Active Damping, Current Estimation**

I. Introduction

Power converters are connected to the grid through damped LC or LCL filters to reduce high-frequency switching harmonics [1]. Indeed, the LC or LCL structure filters out the switching ripple while ensuring the output voltage and current quality meet the grid codes requirements [2], [3]. However, the LCL resonance must be damped to avoid current oscillations in the grid.

A straightforward solution to damp such oscillations is to include a damping resistor in series with the filter capacitor [1]. However, this leads to additional power losses in the filter, thereby impacting the converter efficiency [4]–[6].

The Active Damping (AD) approach is a well-established solution in the literature for reducing the damping resistance while maintaining a damped system response [5], [6]. Indeed, the authors in [6] demonstrate how two main quantities can be utilised to reduce the resonant peak: the capacitor voltage [7]–[9] and current [6], [10], [11]. While the AD with the capacitor current can be implemented through a proportional term [10], a derivative compensator must be applied to the capacitor voltage to ensure adequate damping [6], [10]. Consequently, different approaches are proposed in the literature to avoid amplifying high-frequency noise caused by the derivative term [7]–[9]. For instance, a high-pass filter-based approach is presented in [7], while a lead-lag filter is proposed in [9]. Nevertheless, the voltage-based AD can be sensitive to time delays and discretization techniques [6], [9], [12].

On the other hand, the AD with the capacitor current requires additional sensors [6], thus increasing the hardware architecture complexity and total cost [11]. To this end, the literature provides control algorithms to avoid the installation of extra current sensors. For instance, an observer-based control is implemented in [13]–[15] to estimate the capacitor current. Although some estimation approaches are available, they often feature complex implementations or are sensitive to parameter variations [13]–[15]. To this purpose, this paper proposes a current sensorless AD strategy based on a simple proportional-resonant estimator, providing a straightforward design of its coefficients.

Moreover, the analog-to-digital conversion and PWM delays have a significant impact on the AD control [6]. Indeed, the time delay determines an additional inductive component, thus varying the resonant frequency of the controlled system. Furthermore, the overall delay can result in a negative resistance, depending on the resonant frequency value [5], [6], [8]. Consequently, the time delay can lead to unstable operating conditions if the AD parameters are not correctly tuned. Nevertheless, the literature lacks clear guidelines to tune the AD control parameters properly.

Therefore, this paper proposes an AD control and its analysis to damp the LCL resonance. The main contribution of this paper is the design of a simple proportional-resonant estimator for the capacitor current, which is employed as the input signal in the AD algorithm. Moreover, a theoretical analysis is provided to tune the AD coefficient, evaluating the effect

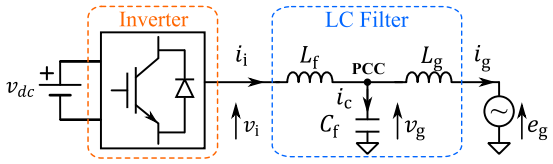

Fig. 1. Schematic overview of a grid-tied inverter.

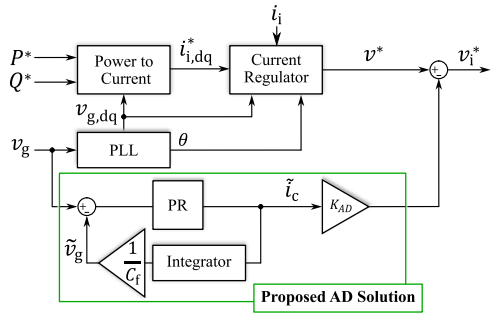

Fig. 2. Block diagram of the proposed active damping (AD) technique integrated into the grid-following control.

of time delays on the damping and resonant frequency of the controlled system. Furthermore, the current estimation is considered to analyse its impact on the system's damping. The effectiveness of the proposed approach is experimentally validated, underlining the significant improvement in the system's damping.

Notably, the proposed AD approach features the following advantages:

- No additional current sensors are required;
- Low sensitivity to output filter parameter uncertainties;
- Reduction of the output filter losses.

The rest of the paper is structured as follows. Section II presents the system under study and the proposed AD solution. The current estimator is described in Section III, along with the tuning procedure for its coefficients. Section IV provides the theoretical analysis for the AD proportional term. In Section V, the proposed AD control is experimentally validated on a three-phase, two-level 30 kVA inverter. Section VI concludes the paper.

II. Overall Control Strategy

The system under study, illustrated in Fig. 1, consists of a three-phase inverter connected to the grid through an LC filter. The grid is modelled as a voltage source e_g in series with its impedance $\bar{Z}_g = R_g + jX_g$, connected to the inverter at the point of common coupling (PCC) with voltage v_g. When considering the grid inductance L_g, the output filter behaves as an LCL filter with a resonant frequency $\omega_{res} = \sqrt{\frac{L_f+L_g}{L_f L_g C_f}}$.

Fig. 2 schematically depicts the proposed AD solution (highlighted in green), which is applied to a conventional grid-following control. More in detail, the inverter injects the power references P^* and Q^*, defined by a higher control level (e.g., maximum power point tracking (MPPT)). The power references are applied through a current control, where the

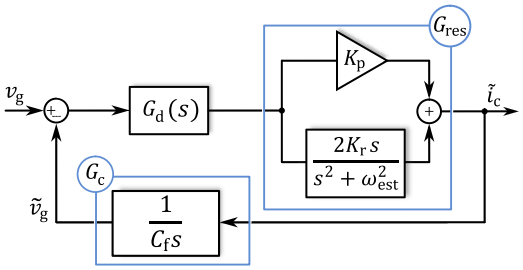

Fig. 3. Small-signal diagram of the capacitor current estimator.

current references $i^*_{d,i}$ and $i^*_{q,i}$ are calculated as in (1) and (2), respectively.

$$i^*_{d,i} = \frac{P^* v_{g,d} + Q^* v_{g,q}}{v^2_{g,d} + v^2_{g,q}} \tag{1}$$

$$i^*_{q,i} = \frac{P^* v_{g,q} - Q^* v_{g,d}}{v^2_{g,d} + v^2_{g,q}} \tag{2}$$

Moreover, the current control consists of a proportional-integral controller implemented in the (d,q) frame rotating at ω_r and tuned based on [1], [16], [17]. The control synchronizes to the grid through a Phase-Lock-Loop (PLL) [17], whose parameters are selected according to [18]. Furthermore, the $d-$axis is aligned to the grid voltage vector (i.e., $v_{g,q} = 0$ pu).

The AD control consists of a proportional coefficient, K_{AD}, which is applied to the estimated capacitor current $\tilde{i}_c$, obtained from the estimator in Fig. 2. More specifically, the estimator comprises a proportional-resonant (PR) cell, whose output represents the estimated capacitor current $\tilde{i}_c$. The PR block operates at approximately zero error through the estimated PCC voltage $\tilde{v}_g$ feedback, which is obtained by integrating $\tilde{i}_c$ and dividining it by the gain C_f. Moreover, the AD algorithm operates in parallel with the conventional control (i.e., applied to the current control output). Therefore, the main control structure can be easily modified as it is independent of the AD algorithm.

III. Capacitor Current Estimator

As discussed in [6], a valuable approach for AD implementation is based on the feedback of the capacitor current. Nevertheless, this strategy requires additional current sensors, thus increasing the total cost. Therefore, this section provides a straightforward method for estimating the capacitor current.

The proposed estimation strategy consists of a proportional resonant cell in (α,β) frame, where the resonant part operates at $\omega_{est} = \omega_{res}$. Fig. 3 illustrates the small-signal diagram of the capacitor current estimation, where $G_d(s)$ and $G_c(s)$ are the time delay and filter capacitor transfer functions, respectively. In more detail, the output of the proportional resonant block is the estimated current $\tilde{i}_c$, which is multiplied by $G_c(s)$, thus obtaining the estimated PCC voltage $\tilde{v}_g$.

The open-loop transfer function of the estimator $G^{est}_{OL}(s)$ is expressed in (3), where $G_{res}(s)$ and $G_c(s)$ are defined in (4) and (5), respectively. Moreover, $G_d(s)$ models the time delay

effect as expressed in (6), where $T_{\rm d} = 1.5T_{\rm sw}$ and $T_{\rm sw}$ is the switching period [19].

$$G_{\rm OL}^{est}(s) = \frac{\tilde{v}_{\rm g}(s)}{v_{\rm g}(s)} = \frac{\tilde{i}_{\rm c}(s)}{i_{\rm c}(s)} = G_{\rm d}(s)G_{\rm res}(s)G_{\rm c}(s) \quad (3)$$

$$G_{\rm res}(s) = K_{\rm p} + \frac{2K_{\rm r}s}{s^2 + \omega_{\rm est}^2} \quad (4)$$

$$G_{\rm c}(s) = \frac{1}{C_{\rm f}s} \quad (5)$$

$$G_{\rm d}(s) = e^{-T_{\rm d}s} \quad (6)$$

The estimation coefficients are tuned considering the open-loop transfer function $G_{\rm OL}^{est}(s)$, for which the crossover frequency $\omega_{\rm crs}$ and phase margin $\Phi_{\rm mar}$ are imposed. To this purpose, the open-loop transfer function is expressed in $j\omega$, as in (7). Note that the time delay effect does not influence the signal magnitude (i.e., $|G_{\rm d}(j\omega)| = 1$).

$$G_{\rm OL}^{est}(j\omega) = e^{-jT_{\rm d}\omega}\left(K_{\rm p} + \frac{j2K_{\rm r}\omega}{-\omega^2 + \omega_{\rm est}^2}\right)\frac{1}{j\omega C_{\rm f}} \quad (7)$$

Let us consider $\omega = \omega_{\rm cross}$ to evaluate the open-loop transfer function $G_{\rm OL}^{est}(j\omega)$ in magnitude and phase. When $\omega = \omega_{\rm cross}$, the resonant part determines an attenuation of $\rho_{\rm r}$ and a phase shift of $-\frac{\pi}{2}$, as pointed out in (8), where $\rho_{\rm r}$ is defined as in (9).

$$G_{\rm res}(j\omega_{\rm crs}) = K_{\rm p} - j\rho_{\rm r} \quad (8)$$

$$\rho_{\rm r} = \frac{2K_{\rm r}\omega_{\rm crs}}{\omega_{\rm crs}^2 - \omega_{\rm est}^2} \quad (9)$$

Next, the open-loop transfer function module $|G_{\rm OL}^{est}(j\omega_{\rm crs})|$ is set as equal to one at $\omega_{\rm cross}$, thus determining the relation in (10).

$$|G_{\rm OL}^{est}(j\omega_{\rm crs})| = 1 \rightarrow K_{\rm p}^2 + \rho_{\rm r}^2 = \omega_{\rm crs}^2 C_{\rm f}^2 \quad (10)$$

Then, the phase of $G_{\rm OL}^{est}(j\omega_{\rm crs})$ is calculated as in (11), where $K_{\rm mar}$ is defined as in (12).

$$\angle G_{\rm OL}^{est}(j\omega_{\rm crs}) = -T_{\rm d}\omega_{\rm crs} - \text{atan}\left(K_{\rm mar}\right) - \frac{\pi}{2} \quad (11)$$

$$\frac{\rho_{\rm r}}{K_{\rm p}} = K_{\rm mar} \quad (12)$$

The phase margin $\Phi_{\rm mar}$ is imposed by applying the condition in (13), from which the expression in (14) is derived.

$$\angle G_{\rm OL}^{est}(j\omega_{\rm crs}) = \Phi_{\rm mar} - \pi \quad (13)$$

$$K_{\rm mar} = \tan\left(-T_{\rm d}\omega_{\rm crs} + \frac{\pi}{2} - \Phi_{\rm mar}\right) \quad (14)$$

When (10) and (14) are combined, the expressions for $K_{\rm p}$ and $K_{\rm r}$ result in (15) and (16), respectively.

$$K_{\rm p} = \frac{C_{\rm f}\omega_{\rm crs}}{\sqrt{1 + K_{\rm mar}^2}} \quad (15)$$

$$K_{\rm r} = C_{\rm f}\left(\omega_{\rm crs}^2 - \omega_{\rm est}^2\right)\frac{K_{\rm mar}}{\sqrt{1 + K_{\rm mar}^2}} \quad (16)$$

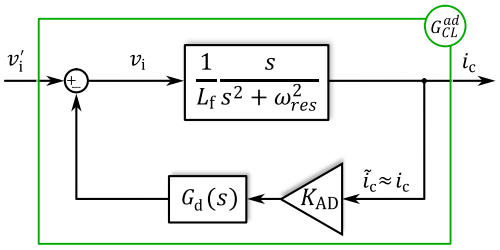

Fig. 4. Small-signal diagram of the proposed AD control.

Note that the resonant frequency of the filter $\omega_{\rm res}$ may be close to the control bandwidth. In this scenario, a high crossover frequency $\omega_{\rm crs}$ and high phase margin $\Phi_{\rm mar}$ cannot be ensured simultaneously. Therefore, a boundary stability condition is derived to correlate $\omega_{\rm crs}$ and $\Phi_{\rm mar}$. Being the estimator unstable for $K_{\rm mar} < 0$ (i.e., $K_{\rm r} < 0$), the condition in (17) needs to be satisfied for the selected $\omega_{\rm crs}$ and $\Phi_{\rm mar}$.

$$K_{\rm mar} > 0 \Rightarrow 0 < T_{\rm d}\omega_{\rm crs} + \Phi_{\rm mar} < \frac{\pi}{2} \quad (17)$$

From (17), the boundary stability condition is derived, resulting in (18).

$$\omega_{\rm crs}^{lim} < \frac{1}{T_{\rm d}}\left(\frac{\pi}{2} - \Phi_{\rm mar}\right) \quad (18)$$

Therefore, given a phase margin $\Phi_{\rm mar}$, the maximum allowed crossover frequency is $\omega_{\rm crs}^{lim}$.

IV. Tuning of the Proposed Active Damping

This section presents a theoretical analysis to select the appropriate AD gain, $K_{\rm AD}$, thus ensuring a well-damped response for the system under study. To this purpose, the control scheme in Fig. 2 is modelled with the small-signal diagram of Fig. 4. For the sake of the analysis, the output inverter voltage is defined as $v_{\rm i}^{'}$ when no AD control is applied, while the actual output inverter voltage is indicated as $v_{\rm i}$. Note that the block diagram in Fig. 4 includes the effect of the time delay, which significantly impacts the tuning of the AD gain [5], [6], [8]. Indeed, the analog-to-digital conversion and PWM delays determine a total delay of $T_{\rm d} = 1.5T_{\rm sw}$ [19]. Therefore, the total delay is modelled in the continuous frequency domain as in (6).

At this stage, the dynamic behaviour of the estimation block is neglected (i.e., the estimator perfectly tracks the capacitor current $G_{\rm CL}^{est}(s) \approx 1$). Note that the resistive elements are neglected, thereby underestimating the actual damping. Based on the small-signal diagram in Fig 4, the closed-loop transfer function $G_{\rm CL}^{ad}(s)$ is obtained, resulting in (19).

$$G_{\rm CL}^{ad}(s) = \frac{i_{\rm c}(s)}{v_{\rm i}^{'}(s)} = \frac{1}{L_{\rm f}}\frac{s}{s^2 + \omega_{\rm res}^2 + \frac{1}{L_{\rm f}}K_{\rm AD}G_{\rm d}(s)s} \quad (19)$$

As it emerges from (19), the gain $K_{\rm AD}$ determines an additional damping term, which depends on $G_{\rm d}(s)$.

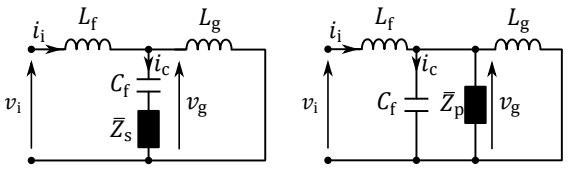

Fig. 5. Impedance model of the active damping term: series (a) and parallel (b) representations.

A. Equivalent Impedance Model

The damping term is typically modelled as an additional impedance in series $\bar{Z}_s$ or parallel $\bar{Z}_p$ to the filter capacitor C_f, as illustrated in Fig. 5a and Fig. 5b [10]. The corresponding transfer functions for series and parallel representation are equal to (20) and (21), respectively.

$$G_s(s) = \frac{i_c(s)}{v_i(s)} = \frac{1}{L_s} \frac{s}{s^2 + \omega_{res}^2 + \frac{L_f + L_g}{L_f L_g} \bar{Z}_s s} \tag{20}$$

$$G_p(s) = \frac{i_c(s)}{v_i(s)} = \frac{1}{L_s} \frac{s}{s^2 + \omega_{res}^2 + \frac{s}{C_f \bar{Z}_p}} \tag{21}$$

The additional impedance related to the active damping term can be obtained by analogy between $G_{CL}^{ad}(s)$ and the transfer functions in (20) and (21), thus resulting in (22) and (23), respectively.

$$\bar{Z}_s(s) = \frac{L_g}{L_f + L_g} K_{AD} G_d(s) \tag{22}$$

$$\bar{Z}_p(s) = \frac{L_f}{C_f} \frac{1}{K_{AD} G_d(s)} \tag{23}$$

When considering $s = j\omega$, the additional impedance can be expressed in resistive and inductive components, thereby obtaining (24) and (25) for series and parallel representations.

$$R_s = \frac{L_g K_{AD}}{L_f + L_g} \cos(\omega T_d) \quad L_s = -\frac{L_g K_{AD}}{L_f + L_g} \sin(\omega T_d) \tag{24}$$

$$R_p = \frac{L_f}{C_f K_{AD}} \cos(\omega T_d) \quad L_p = \frac{L_f}{C_f K_{AD}} \sin(\omega T_d) \tag{25}$$

The expressions in (24) and (25) highlight the time delay effect, which results in an additional inductive component. Therefore, the resonant frequency of the controlled system is expected to vary depending on K_{AD}. Moreover, the resistive and inductive parts are nonlinearly dependent on ω. Consequently, the system damping cannot be evaluated analytically with the impedance representation. For this reason, the Padè approximation of $G_d(s)$ is considered, as will be presented in the following subsection.

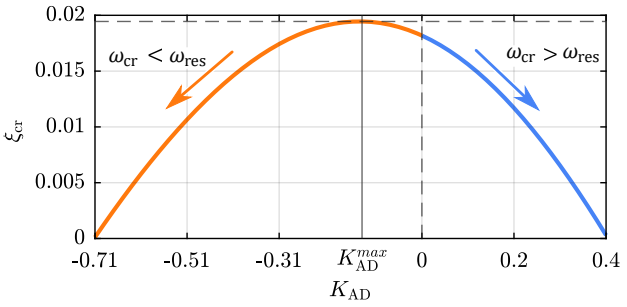

Fig. 6. Critical damping ξ_{cr} to the variation of the AD gain K_{AD}.

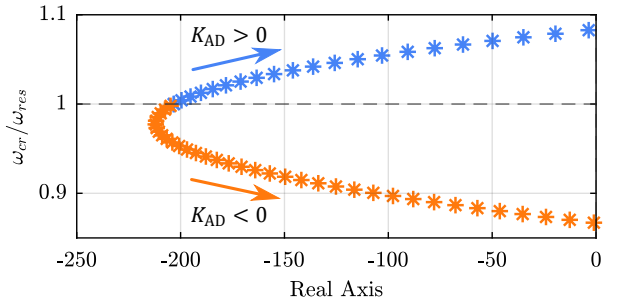

Fig. 7. Placement of the critical pole p_3 to the variation of the AD gain K_{AD}.

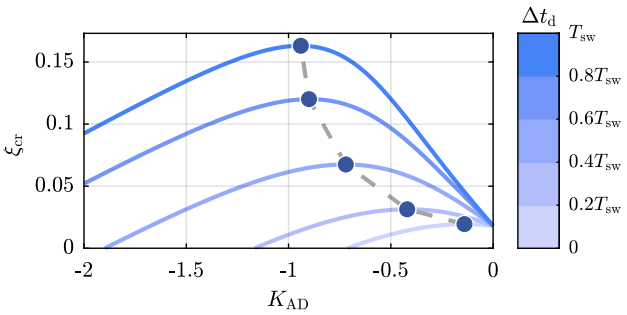

Fig. 8. Critical damping ξ_{cr} to the variation of the AD gain K_{AD} when adding a time delay of Δt_d.

B. Small Signal Analysis

The second-order polynomial approximation in (26) (i.e., Padé approximation [20]) is applied to $G_d(s)$, thus allowing the calculation of the $G_{CL}^{ad}(s)$ damping term.

$$G_d(s) \approx \frac{1 - s\frac{T_d}{2} + s^2\frac{T_d^2}{12}}{1 + s\frac{T_d}{2} + s^2\frac{T_d^2}{12}} \tag{26}$$

By substituting (26) in (19), the closed-loop transfer function features a fourth-order denominator. The denominator is numerically solved for different K_{AD} to study its impact on the damping. Refer to the Appendix for the numerical procedure. The resulting four poles are complex conjugate in pairs as follows:

- $p_1 = \bar{p}_2$, which are located at $|\omega_{p1}| = |\omega_{p2}| > \omega_{res}$. This pair features damping always greater than zero independently on K_{AD};

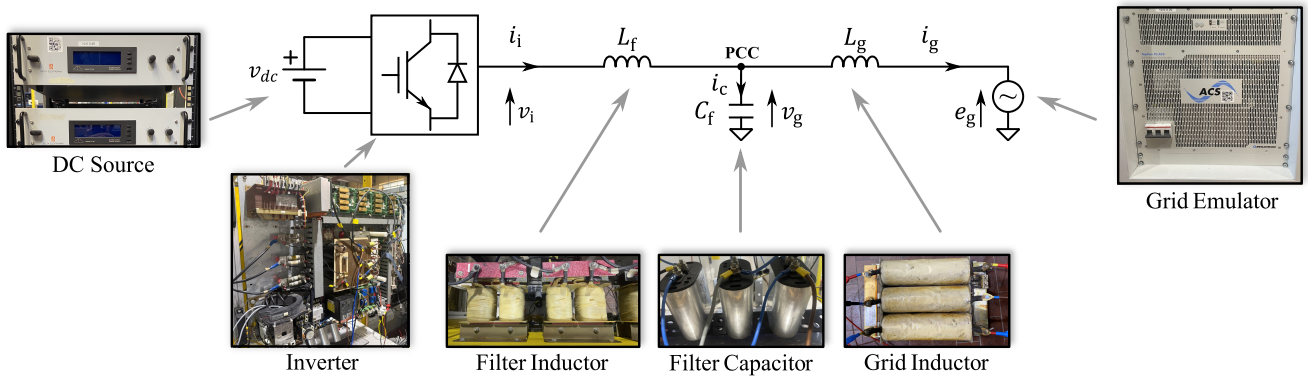

Fig. 9. Experimental setup.

- $p_3 = \bar{p}_4$, located at $|\omega_{p3}| = |\omega_{p4}| < \omega_{res}$. These poles are critical as the damping can be negative depending on K_{AD}.

The variation of the critical damping ξ_{cr} versus the AD gain K_{AD} is shown in Fig. 6. Moreover, Fig. 7 illustrates the placement of the critical pole p_3, while $p_4 = \bar{p}_3$. Three main aspects can be noticed in Figs. 6 and 7:

- A maximum critical damping ξ_{cr}^{max} exists at K_{AD}^{max};
- The resonant frequency ω_{cr} of the critical poles depends on K_{AD} (i.e., $\omega_{cr} < \omega_{res}$ for $K_{AD} < 0$ (orange curve), whereas $\omega_{cr} > \omega_{res}$ for $K_{AD} > 0$ (blue curve));
- The critical poles do not distribute uniformly to a variation ΔK_{AD}, as illustrated in Fig. 7. Indeed the critical poles move quickly to the unstable area for $K_{AD}^{max} + \Delta K_{AD}$ but tend to remain in the stable area for $K_{AD}^{max} - \Delta K_{AD}$.

Therefore, K_{AD} should be selected lower than K_{AD}^{max} (i.e., $K_{AD}^{max} - \Delta K_{AD}$), at which a lower resonant frequency is expected for the system under study.

C. Sensitivity to Capacitor Current Estimation

In Section IV-B, the current estimator is neglected, assuming a perfect tracking of the capacitor current. However, the estimated $\tilde{i}_c$ and actual i_c currents may differ in phase and module (i.e., delay in time and attenuation). For instance, an error in the estimated current can occur when $\omega_{est} \neq \omega_{res}$ (e.g., due to wrong parameter estimation). Therefore, the estimator needs to be considered as the damping term strictly depends on time delays.

For this purpose, the critical poles are calculated assuming an additional delay Δt_d in (26), where the Δt_d represents the delay caused by the current estimator. Fig. 8 shows the critical damping to the variation of K_{AD} when adding a time delay up to the switching period. When increasing Δt_d, the maximum critical damping ξ_{cr}^{max} moves to higher values for higher $|K_{AD}|$, as illustrated in Fig. 8.

Therefore, the current estimation improves the system damping as the maximum critical damping ξ_{cr}^{max} increases, moving to higher values of $|K_{AD}|$. As a consequence, a higher system damping is expected for the same K_{AD} when $\tilde{i}_c$ features a time delay. Note that an attenuation of the estimated current does not influence the maximum critical damping ξ_{cr}^{max} but only the K_{AD}^{max}.

TABLE I
EXPERIMENTAL SETUP PARAMETERS.

Inverter		**Base Values**		**Grid**	
S_N	30 kVA	S_{base}	30 kVA	$\hat{V}_g$	$120\sqrt{2}$ V
V_{DC}	400 V	V_{base}	$120\sqrt{2}$ V	L_g	0.0609 pu
f_{sw}	10 kHz	ω_{base}	314 rad/s	R_g	0.0075 pu
AD				**LC Filter**	
K_p	0.842 pu	K_{AD}	-1 pu	L_f	0.0480 pu
K_r	19.944 pu	f_{res}	1.78 kHz	C_f	0.0299 pu

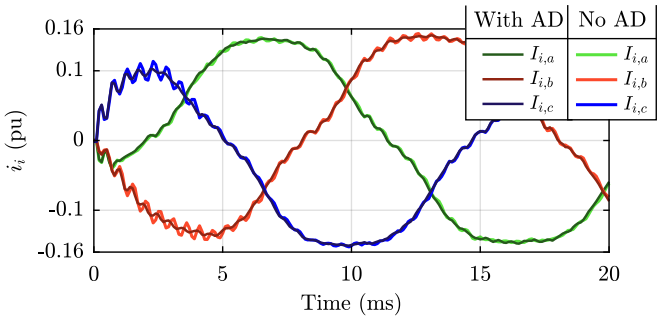

Fig. 10. Three-phase inverter-side current i_i with and without the proposed AD solution.

V. EXPERIMENTAL VALIDATION

Fig. 9 schematically illustrates the tested system along with the experimental setup consisting of a 30 kVA, three-phase, two-level inverter connected to a grid emulator with an LC filter and a grid inductor. An ideal DC source supplies the inverter, which is controlled by a dSpace platform. Table I summarizes the main system and control parameters.

Based on the analysis in Section IV, the proposed AD strategy is expected to improve the system damping. Moreover, the current estimator should increase the critical damping, as discussed in Section IV-C. Therefore, the capacitor current is measured to evaluate the current estimator and validate its effect on the system damping. Note that no additional resistors are included in the LC filter for the experimental validation.

The test consists of applying a reactive power reference step Q^* of 0.15 pu (i.e., $i_q^* = 0.15$ pu) to trigger the resonant

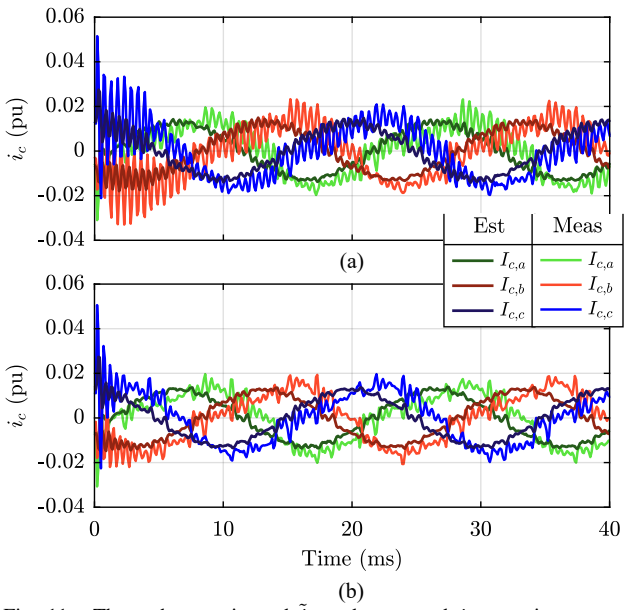

Fig. 11. Three-phase estimated $\tilde{i}_c$ and measured i_c capacitor current: (a) without and (b) with the proposed AD solution.

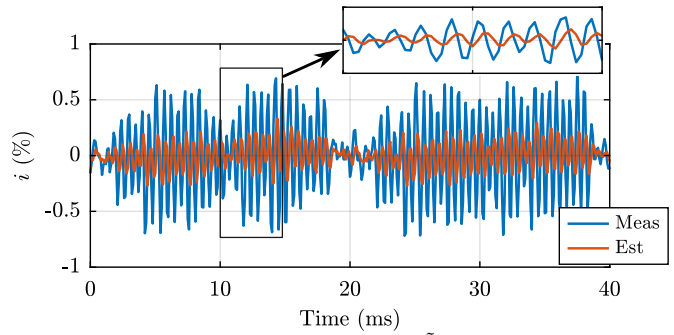

Fig. 12. High frequency component of estimated $\tilde{i}_c$ and measured i_c capacitor current without the proposed AD solution.

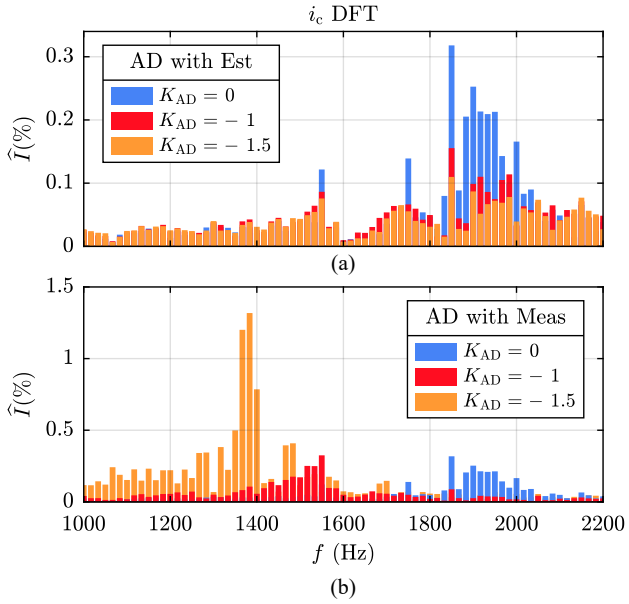

Fig. 13. Harmonic contents of the measured capacitor current i_c for different K_{AD} values: (a) when utilizing the estimated current $\tilde{i}_c$, and (b) when utilizing the measured current i_c in the AD control.

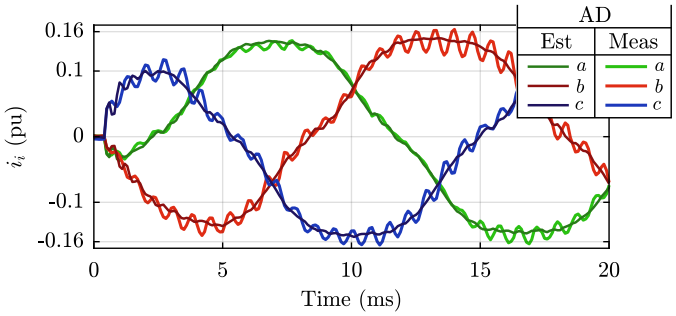

Fig. 14. Three-phase inverter-side current i_i when cosidering the estimated $\tilde{i}_c$ and measured i_c capacitor current for $K_{AD} = -1.5$.

frequency of the LCL. As shown in Fig. 10, the system damping is significantly improved when the proposed AD control is applied. Indeed, the inverter-side current in Fig. 10 features lower oscillation for $K_{AD} = -1$. Furthermore, the estimated and measured capacitor currents are displayed in Fig. 11, where two main aspects can be observed:

- The measured capacitor current is significantly more dampened when applying the AD control, as shown in Fig. 11b;
- The estimated and measured capacitor currents differ in phase and magnitude.

Even though a phase shift appears at the fundamental frequency, the main purpose of the estimator is to track the high-frequency component (i.e., close to the resonant frequency). Therefore, the estimated and measured currents are compared by observing the high-frequency component. As shown in Fig. 12, the estimated current follows the measured one with a time delay of $\Delta t_d = 0.1$ ms.

Nevertheless, the time delay is expected to improve the damping for the same K_{AD} value, as presented in Section IV-C. Therefore, the control in Fig. 2 is modified by utilising the measured current instead of the estimated one to compare the system response for the same K_{AD}. As can be observed in Fig. 13a, the high-frequency component peak is reduced (i.e., increase in damping) when applying the proposed AD strategy with the estimated capacitor current $\tilde{i}_c$ (i.e., $\Delta t_d \neq 0$). Moreover, the harmonic content moves slightly to lower frequency values. On the other hand, the resonant frequency significantly decreases to lower values when utilising the measured capacitor current i_c, as illustrated in Fig. 13b. For $K_{AD} = -1$ (marked in red), the resonant peak is higher when considering the measured current (0.32 %) instead of the estimated one (0.15 %). As can be seen in Fig. 13b, the system damping is considerably reduced when applying the measured current i_c and $K_{AD} = -1.5$ (marked in orange), leading to unstable operating conditions. Indeed, the current oscillations after the step increase over time, as shown in Fig. 14.

VI. Conclusion

The paper proposes an AD solution based on a simple current estimator, providing a straightforward method for selecting the estimator parameters. The effect of the AD proportional

coefficients is comprehensively analyzed to tune the control properly and investigate the impact of time delays. Moreover, the current estimator is considered to evaluate its effect on the system damping. The performed analysis demonstrates how the estimation delay improves the critical damping of the system. The proposed AD strategy is experimentally validated, showing consistent results that align with theoretical considerations. Indeed, the proposed control improves the system's damping when the current estimator is employed. On the other hand, using the measured capacitor current may decrease system damping for the same AD parameter. Therefore, the proposed AD strategy represents a robust and straightforward solution that allows the reduction of resistive components in the LC and LCL filters without requiring additional sensors.

APPENDIX

The denominator of the approximated closed-loop transfer function can be written as in (27), where the coefficients are specified in (28), (29), (30), and (31).

$$G_{\mathrm{CL}}^{ad}(s) \approx \frac{1}{L_{\mathrm{s}}} \frac{s\left(1 + s\frac{T_{\mathrm{d}}}{2} + s^2\frac{T_{\mathrm{d}}^2}{12}\right)}{as^4 + bs^3 + cs^2 + d} \tag{27}$$

$$a = \left(\frac{T_{\mathrm{d}}}{2} + \frac{K_{\mathrm{AD}}}{L_{\mathrm{f}}}\frac{T_{\mathrm{d}}^2}{12}\right)\frac{12}{T_{\mathrm{d}}^2} \tag{28}$$

$$b = \left(1 + \omega_{\mathrm{res}}^2\frac{T_{\mathrm{d}}^2}{12} - \frac{K_{\mathrm{AD}}}{L_{\mathrm{f}}}\frac{T_{\mathrm{d}}}{2}\right)\frac{12}{T_{\mathrm{d}}^2} \tag{29}$$

$$c = \left(\omega_{\mathrm{res}}^2\frac{T_{\mathrm{d}}}{2} + \frac{K_{\mathrm{AD}}}{L_{\mathrm{f}}}\right)\frac{12}{T_{\mathrm{d}}^2} \tag{30}$$

$$d = \omega_{\mathrm{res}}^2\frac{12}{T_{\mathrm{d}}^2} \tag{31}$$

The denominator in (27) can be written as in (32) and imposed equal to zero.

$$\left(s^2 + \frac{a^2}{2}s\right)^2 = \left(\frac{a^2}{4} - b\right)s^2 - cs - d \tag{32}$$

Then, the auxiliary variable y is introduced to complete the square, thus reducing the fourth-order into a second-order equation. If the condition in (34) is verified, the expression in (33) is a square of a binomial. The condition in (34) determines a third-order equation in y, solved by applying the Cardano method [21].

$$\left(s^2 + \frac{a^2}{2}s + \frac{y}{2}\right)^2 = \left(\frac{a^2}{4} - b + y\right)s^2 - \left(c - \frac{1}{2}ay\right)s - d + \frac{y^2}{4} \tag{33}$$

$$\left(c - \frac{1}{2}ay\right)^2 = 4\left(\frac{a^2}{4} - b + y\right)\left(-d + \frac{y^2}{4}\right) \tag{34}$$

Once that y is calculated, the obtained value is replaced in (33) to solve the second-order equation.

REFERENCES

[1] S. N. Vukosavic, *Grid-side converters control and design*. Springer, 2018.

[2] Terna, "Code for Transmission Dispatching. Development and Security of the Grid," Grid Code, Mar. 2023.

[3] Transmission, D. C. of the IEEE Power, and E. Society, *IEEE519-2022, IEEE Standard for Harmonic Control in Electric Power Systems*, Std., May 2022.

[4] C. Zhuo, X. Zhang, W. Song, and H. Yi, "Active resonant damper with control strategy based on inverter output conductance optimization under weak grid conditions," *IEEE Journal of Emerging and Selected Topics in Power Electronics*, 2024.

[5] W. Guo, T. Chen, and A. Q. Huang, "A control bandwidth optimized active damping scheme for LC and LCL filter-based converters," *IEEE Access*, vol. 11, pp. 34 286–34 296, 2023.

[6] J. Dannehl, F. W. Fuchs, S. Hansen, and P. B. Thøgersen, "Investigation of active damping approaches for PI-based current control of grid-connected pulse width modulation converters with lcl filters," *IEEE Transactions on Industry Applications*, vol. 46, no. 4, pp. 1509–1517, 2010.

[7] M. Malinowski and S. Bernet, "A simple voltage sensorless active damping scheme for three-phase PWM converters with an LCL filter," *IEEE Transactions on Industrial Electronics*, vol. 55, no. 4, pp. 1876–1880, 2008.

[8] E. Matijevic, R. Sharma, F. Zare, and D. Kumar, "Extremum seeking as a tool for active damping of active front-end converters," *IEEE Transactions on Industrial Electronics*, vol. 70, no. 4, pp. 3404–3413, 2022.

[9] R. Peña-Alzola, M. Liserre, F. Blaabjerg, R. Sebastián, J. Dannehl, and F. W. Fuchs, "Systematic design of the lead-lag network method for active damping in LCL-filter based three phase converters," *IEEE Transactions on Industrial Informatics*, vol. 10, no. 1, pp. 43–52, 2013.

[10] S. Li and H. Lin, "A capacitor-current-feedback positive active damping control strategy for LCL-type grid-connected inverter to achieve high robustness," *IEEE Transactions on Power Electronics*, vol. 37, no. 6, pp. 6462–6474, 2021.

[11] N. Upadhyay, N. P. Padhy, and P. Agarwal, "Grid-current control with inverter-current feedback active damping for LCL grid-connected inverter," *IEEE Transactions on Industry Applications*, vol. 60, no. 1, pp. 1738–1749, 2023.

[12] Y. Li, J. Gao, Z. Zhang, and Q. Wang, "Model-based and model-free predictive active damping for LCL-type active-front-end rectifiers," *IEEE Transactions on Industrial Electronics*, vol. 71, no. 10, pp. 11 754–11 765, 2024.

[13] M. Awal and S. Schröder, "Sensorless active damping in switching frequency constrained medium voltage multi-megawatt grid forming converters," in *2022 IEEE Applied Power Electronics Conference and Exposition (APEC)*, pp. 1419–1424. IEEE, 2022.

[14] V. Miskovic, V. Blasko, T. Jahns, R. Lorenz, and H. Zhang, "Robust sensorless control of grid connected converters with LCL line filters using frequency adaptive observers as AC voltage estimators," in *2016 IEEE Applied Power Electronics Conference and Exposition (APEC)*, pp. 2167–2174. IEEE, 2016.

[15] V. Miskovic, V. Blasko, T. M. Jahns, A. H. Smith, and C. Romenesko, "Observer-based active damping of LCL resonance in grid-connected voltage source converters," *IEEE Transactions on Industry Applications*, vol. 50, no. 6, pp. 3977–3985, 2014.

[16] F. Blaabjerg, *Control of Power Electronic Converters and Systems: Volume 2*, vol. 2. Academic Press, 2018.

[17] F. Blaabjerg, R. Teodorescu, M. Liserre, and A. V. Timbus, "Overview of control and grid synchronization for distributed power generation systems," *IEEE Transactions on industrial electronics*, vol. 53, no. 5, pp. 1398–1409, 2006.

[18] S.-K. Chung, "A phase tracking system for three phase utility interface inverters," *IEEE Transactions on Power electronics*, vol. 15, no. 3, pp. 431–438, 2000.

[19] S. Buso and P. Mattavelli, *Digital control in power electronics*. Springer Nature, 2022.

[20] G. A. Baker Jr and J. L. Gammel, "The padé approximant," *Journal of Mathematical Analysis and Applications*, vol. 2, no. 1, pp. 21–30, 1961.

[21] J. S. Chahal, "Solution of the cubic," *Resonance*, vol. 11, no. 8, pp. 53–61, 2006.